Research Paper
J. Astron. Space Sci. 43(3), 157-167 (2026)
https://doi.org/10.5140/JASS.2026.43.3.157

JASS Journal of Astronomy and Space Sciences

ShadowCam Establishes Faustini's Ancient Age

Barbara Giuri[1†], Carolyn H. van der Bogert[2,3], Mark Robinson[1]

[1]Intuitive Machines, Phoenix, AZ 85004, USA
[2]Institut für Planetologie, Universität Münster, Münster 48149, Germany
[3]Directorate of Human and Robotic Exploration, European Space Agency (ESA), European Space Research and Technology Centre (ESTEC), Noordwijk, 2201 AZ, The Netherlands

ShadowCam is a NASA-funded imaging experiment onboard the Korea Pathfinder Lunar Orbiter (also known as Danuri), providing high-resolution (2 m/pixel) images of permanently shadowed regions (PSRs), enabling investigations into the distribution and accessibility of water ice and other volatiles necessary for future human exploration. Here, we use a ShadowCam image mosaic to revisit the crater-size frequency distribution (CSFD) of Faustini crater floor, the third-largest PSR, and of high cold-trapping potential. We find that all count areas exhibit crater equilibrium over the entire diameter range (< 2 km), hence supporting an ancient age for the Faustini impact and surface floor materials. In addition, we estimate the amount of basin ejecta material delivered to Faustini crater from the Imbrium, Orientale, and Schrödinger formation events using an ejecta distribution model to investigate the origin of a previously identified disturbance in the CSFD. As expected, the model originally developed for simple and complex craters yielded inconsistent results, underscoring the need for further studies and a deeper understanding of ejecta thickness distribution for the basin-sized impact regime.

Keywords: ShadowCam, Korea Pathfinder Lunar Orbiter (KPLO), Lunar Reconnaissance Orbiter (LRO), Ejecta thickness models, Impacts, rater size-frequency distribution

1. INTRODUCTION

The work presented here extends the results presented in Giuri et al. (2024), in which the authors investigated the model ages and origin(s) of plains and crater-floor materials in the lunar circum-south polar region, finding that smooth deposits formed by ballistic emplacement from multiple basin- and crater-forming events over a period between ~3.8 and ~2.5 Ga ago. They found that crater floor units exhibited distinctive crater-size frequency distributions (CSFDs) associated with a disturbance or partial resurfacing of craters up to around 500 m across the Haworth and Faustini floors, while Shoemaker exhibited complete resurfacing (Fig. 1 after Giuri et al. 2024, Figs. 2(a)–2(c)). The origin of the disturbance or the cause of the partial resurfacing for two rather than all three neighboring craters remained unclear. However, possibilities include (1) resolution limitations of the data set used, (2) an unknown geologic process, or both.

Here, we use CSFD analysis derived from a ShadowCam controlled mosaic to estimate the relative age of Faustini crater and the thickness of basin ejecta material deposited on the Faustini floor from the last three largest basins: Imbrium, Orientale, and Schrödinger.

1.1 Crater Statistics Using ShadowCam

ShadowCam is a NASA Advanced Exploration Systems (AES) funded instrument onboard KPLO, Korea Pathfinder Lunar Orbiter satellite, aimed at providing insights into polar regions and the distribution and accessibility of surface volatiles including water ice (Robinson et al. 2023; Humm et al. 2023). The design is inherited from Lunar Reconnaissance Orbiter Camera (LROC) Narrow Angle Camera (NAC) (Robinson et al. 2010; Humm et al. 2016; Speyerer et al. 2016) but optimized to image within permanently shadowed regions (PSRs). The modifications

Received 13 MAY 2026 **Revised** 25 JUL 2026 **Accepted** 04 SEP 2026
†**Corresponding Author**
Tel: +1-417-396-1667, E-mail: bgiuri@intuitivemachines.com
ORCID: https://orcid.org/0009-0006-0187-3112

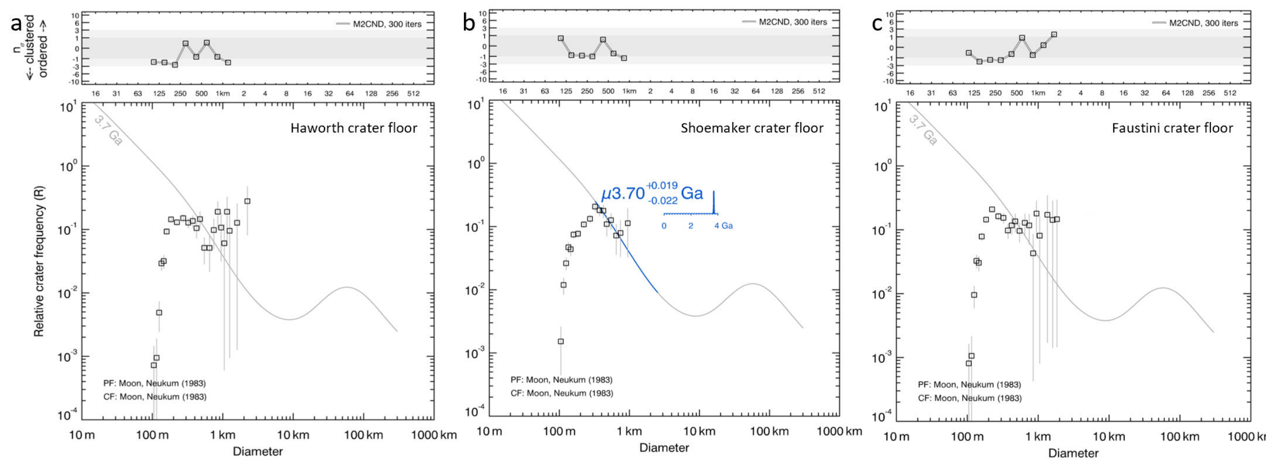

Fig. 1. Crater-size frequency distribution (CSFD) R-plots for Haworth, Shoemaker, and Faustini crater floors. Adapted from Giuri et al. (2024) with CC BY-ND-NC.

provide for an increased integration time enabled with a time delay integration detector (TDI) that allows high average S/N ratio (100) within PSRs (Robinson et al. 2010, 2023). These modifications allow ShadowCam to provide unprecedented high-sensitivity and high-resolution images at 1.7 m/pixel scale from 100 m altitude in line with its science and exploration objectives (Robinson et al. 2023; Humm et al. 2023). PSRs never see direct sunlight. Instead, they receive secondary scattered light reflected off topographic highs (Watson et al. 1961; Shoemaker et al. 1994; Gläser et al. 2018; Thompson et al. 2019; Mahanti et al. 2022; O'Brien & Byrne 2022). This diffuse, indirect illumination creates a complex lighting geometry challenging geologic interpretations (Mahanti et al. 2022; Speyerer et al. 2023). Despite ShadowCam providing high-resolution views into the shadows potentially revealing albedo contrasts for ice detection, regolith properties, terrain roughness, and subtle morphological features undetected with other datasets (i.e., hillshades), the diffuse lighting may alter the appearance of other landforms such as craters introducing significant biases to the crater size-frequency distribution analysis and model age derivation (Sonke et al. 2025; Speyerer et al. 2026). Thus, due to the multiple photometric angles contributing to the illumination within the PSR (Mahanti et al. 2022) careful consideration is required when using ShadowCam datasets for crater measurements. Consequently, a multi-image approach of ShadowCam, LROC NACs and DTMs is necessary to mitigate measurement error and interpret surface geology (Speyerer et al. 2024).

1.2 Ejecta Thickness Modeling

Impact craters are a ubiquitous landform across the Moon. During the final stage of crater formation, material is ballistically ejected along a parabolic trajectory until it hits the surface, forming the ejecta blanket (Melosh 1989). The topography and morphology of ejecta blankets will vary with distance from the impact, the pre-existing surface, and impactor characteristics (Melosh 1989). Large (≥ 300-km-diameter) craters are called basins as defined by Hartmann & Wood (1971). They eject substantial amounts of material that distribute across the Moon, resulting in varying degrees of mixing with local materials (Oberbeck et al. 1974). Modeling the amount and distribution of basin material spread around the Moon is highly dependent on the correct estimation of basin diameters and that of the transient crater – the initial cavity that opens during the excavation stage of crater formation (Croft 1985; Melosh 1989; Cintala & Grieve 1998). Several studies attempted to derive/model how much material is excavated and distributed across the Moon based on terrestrial and lunar craters, on impact scaling laws (McGetchin et al. 1973; Pike 1974, 1977; Housen et al. 1983), and ejecta decay rates (McGetchin et al. 1973; Petro & Pieters 2004, 2006, 2008; Fassett et al. 2011) with variable results. Thus, basin and transient crater diameters, along with the degree of mixing with local materials and other parameters, remain poorly understood (Austin et al. 2024). A comprehensive overview of the different models can be found in the Petro & Pieters (2004) series and their limitations in Austin et al. (2024). Here, we focus on providing a first-degree estimate of the ejecta thickness from the last three basins that was emplaced within Faustini using Pike (1974) model as our case study, while the thickness within Haworth and Shoemaker using the equations of Pike (1974), McGetchin et al. (1973), and Housen et al. (1983) are reported in the Appendix (Table A1 and A2). Other models have been developed that for example measure ejecta mass and velocity distributions via point-source scaling models (Holsapple & Schmidt 1987; Holsapple 1993; Housen & Holsapple 2011) that can be used to estimate ejecta thickness using elliptic ballistic trajectories following Dobrovolskis (1981). However, here we only aim at providing a first-degree estimate of ejecta thickness by using more intuitive equations that, although originally developed for simple and complex craters, serve as benchmarks in ballistic sedimentation models (Xu et al. 2024).

2. DATA AND METHODS

We undertook two studies testing the origin of the Faustini crater floor CSFD disturbance.

(1) The CSFD in Giuri et al. (2024) was derived from a 20 m/pixel LDEM generated hillshade (Smith et al. 2010). Hillshade datasets are ideal for polar investigations because they remove the effects of shadowing thus facilitating morphologic interpretations. However, hillshades can preclude the identification of subtle surface features that may be included in the count area. Here, we tested the robustness of the crater statistics using a ShadowCam controlled-image mosaic of the Faustini crater floor (Grieser et al. 2025; Collins et al. 2026), allowing for greater accuracy in area selection and, in principle, crater measurements due to the higher spatial resolution (Figs. 2 and 3). The mosaic was generated using multiple overlapping images with consistent illumination geometry acquired on sequential orbits and controlled using similar methods to those used to control LROC NAC mosaics (Klem et al. 2014; Grieser et al. 2024).

(2) We explore the potential relationship between basin ejecta thickness within Faustini and the origin of the disturbance. By estimating basin ejecta thickness, we aim to (a) constrain how much, if any, material reached the area of interest, and (b) test the inferred 3.7 Ga Orientale age for Haworth, Shoemaker, and Faustini crater floor materials (Giuri et al. 2024). We used the Pike (1974) equation to constrain ejecta thickness. We compared the results using

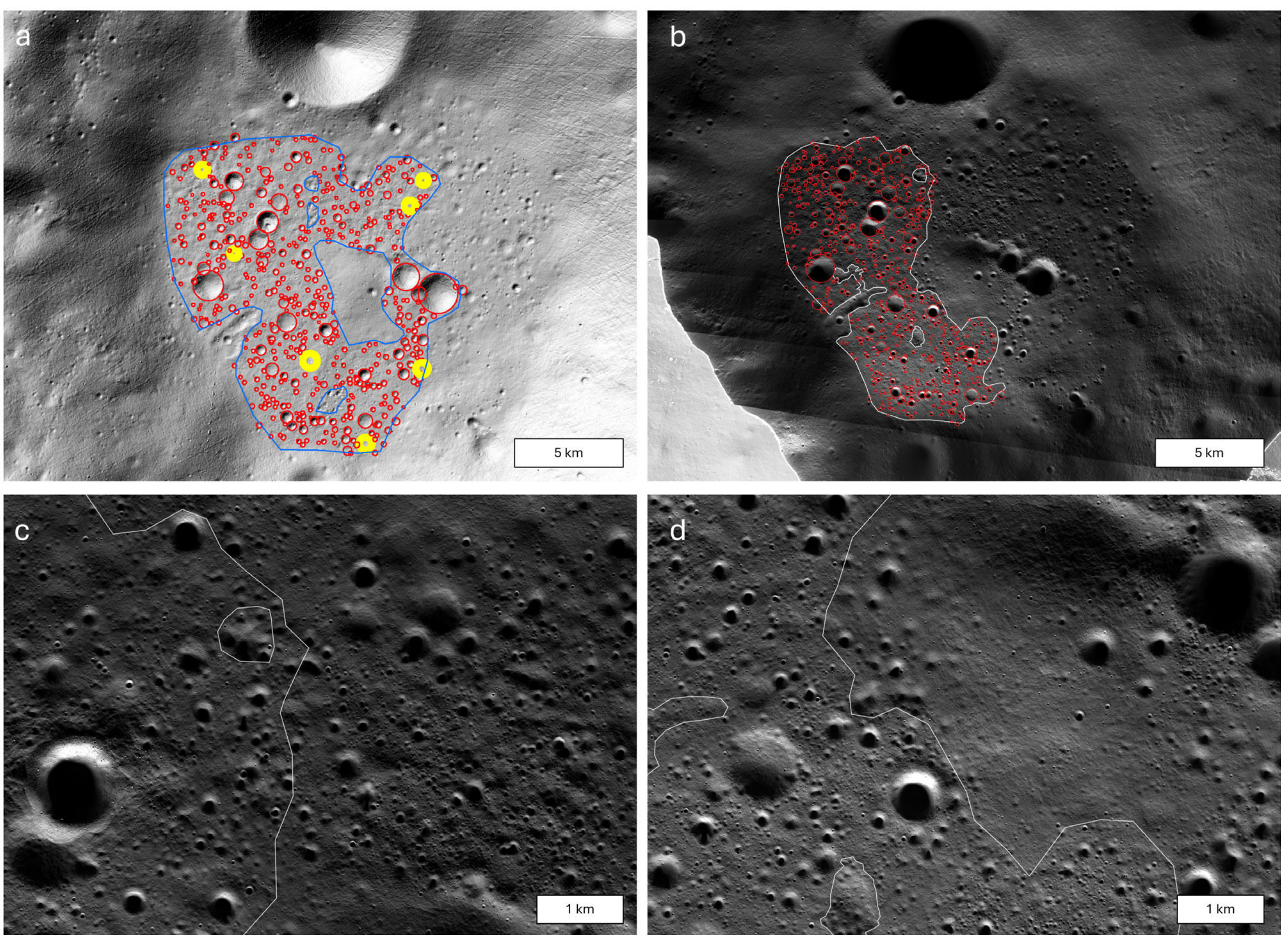

Fig. 2. Faustini floor count areas over (a) the LDEM generated hillshade used by Giuri et al. (2024), and (b) using ShadowCam mosaic in this work. Panels (c) and (d) show the morphologic units we were able to identify and separate from the count area using ShadowCam for example Elephant Hide Texture that was previously included.

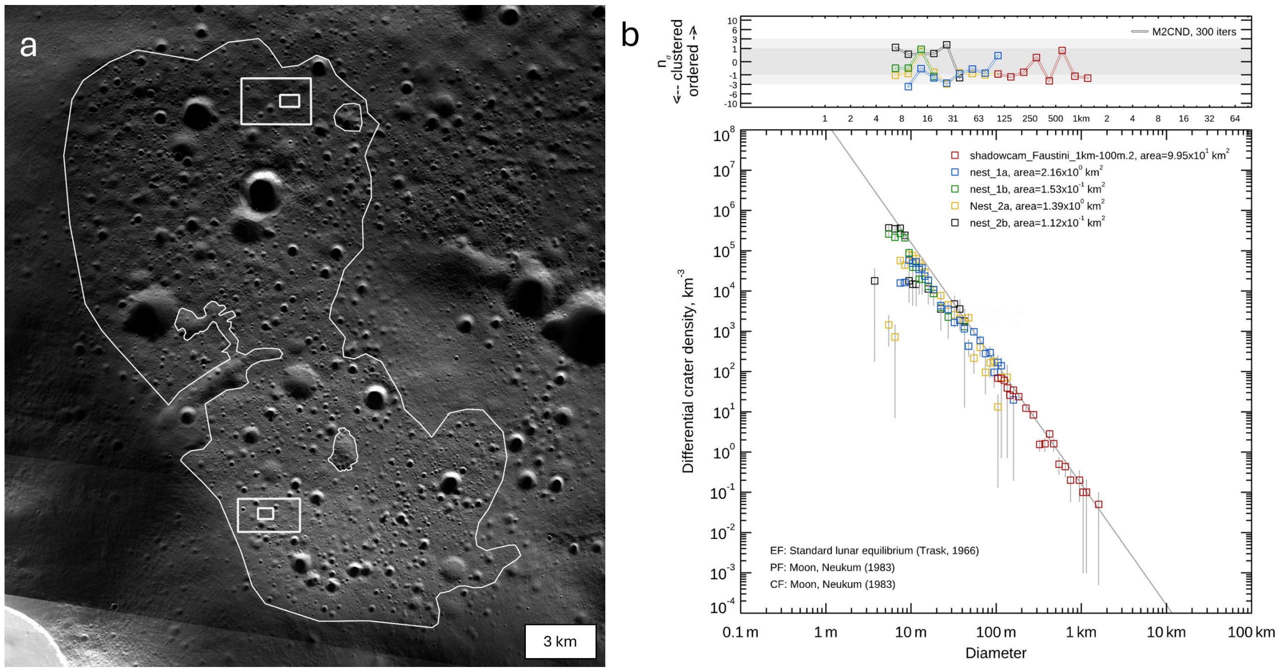

Fig. 3. Nested CSFD measurement approach adopted in this work showing five count areas (a), and (b) crater-size frequency distribution (CSFD) differential representation of all areas exhibiting crater equilibrium across all diameters.

methods presented in McGetchin et al. (1973), and Housen et al. (1983), see the Appendix (Table A2). We adjusted Pike's equation to account for the curvature of the Moon by substituting the distance (r) with angular distances (α), and we omitted the Oberbeck et al. (1974) local to foreign basin material mixing ratio from our estimates to avoid potential overestimations as well as the need to apply adjustments or permutations to the original equation to account for a specific geological setting (Pieters et al. 1985; Blewett et al. 1995; Petro & Pieters 2004). Finally, we relied on basin diameters from Neumann et al. (2015), who used GRAIL and LOLA data, and transient crater diameters (Mean TC radius) from Wieczorek & Phillips (1999) and Petro & Pieters (2004), who used geophysical data from the Clementine mission as empirical physical evidence rather than using the Melosh (1989) scaling law. The Melosh (1989) scaling law is well established for simple (0.85 factor) and complex craters (0.6 factor), while basins warrant consideration as a separate regime. Basins undergo extensive catastrophic modification such as structural collapse, fracturing, ring formation, and isostatic rebound, which violate the assumptions of π-scaling used in the Melosh model. Thus, using Melosh (1989) scaling law can result in an under- or overestimation of the transient crater diameter. Instead, gravity data allows for an accurate reconstruction of the transient crater diameter and excavation depth as gravity signatures are preserved deep in the crust (Neumann et al. 2015).

2.1 Crater Statistics

Similar to the work of Giuri et al. (2024), we used QGIS to manually select a homogeneous count area within the Faustini crater floor in ShadowCam mosaic, avoiding large secondary clusters (e.g., Neukum et al. 2001; McEwen & Bierhaus 2006; Hiesinger et al. 2011, 2023). Given the higher resolution of the mosaic compared to the hillshade, our refined count area mostly overlaps with the Lower floor unit as mapped by Williams et al. (2024). To improve crater-counting efficiency, we adopted a nested approach with decreasing crater diameters. Our main count area includes crater diameters ranging from ≥ 1 km to 100 m. Two large nests within the main count areas have crater diameters of ~100 m to ≥ 10 m, and within these two large nests, we selected two smaller nests with remaining craters < 10 m in diameter (Fig. 3(a)). CSFD measurements of primary craters were made using the QGIS plugin OpenCraterTool (Heyer et al. 2023), while fitting, randomness, and Poisson error analysis were conducted in CraterStats (Michael & Neukum 2010; Michael et al. 2016) using the production (PF) and chronology (CF) functions of Neukum (1983).

2.2 Basin Ejecta Estimates

To estimate the amount of basin materials at a given location, we used the Pike (1974) model in which he revisited the ejecta thickness at the rim from McGetchin's model to derive the relation:

$$t = T(r/R)^{(-B)} \quad (1)$$

where t is the thickness of the material, T is the thickness of the ejecta at the rim, r is the distance from the center of a basin or crater to the area of interest – or α in our case, R is the radius of the transient crater for large impacts – or *Mean TC radius* here, and B is the decay constant of 3.0 ± 0.5 as a standardized best fit value (Melosh 1989; Austin et al. 2024). For both models the equation is the same except for the value of T. While in McGetchin et al. (1973) T is defined as $T = 0.14\ R^{(0.74)}$, for Pike (1974) T is defined as:

$$T = 0.033\ R \quad (2)$$

Here, we use Pike (1974) Eqs. (1) and T value (2) to constrain ejecta thickness (Table 1, A1, and A2).

3. RESULTS

We present a refined, albeit smaller, count area in terms of homogeneity where we were able to identify and exclude different features and surface textures such as Elephant Hide Textures (EHTs) (Fig. 2).

Differently from conventional crater counting methodologies where all visible primary craters are measured within a count area, we divided the main count area into nests with decreasing crater diameters (Figs. 3(a) and A1). We find that the main area and all nests exhibit CSFDs with slopes of –2, indicative of crater equilibrium (Trask 1966) across the entire measured crater diameter range such that absolute model ages (AMAs) could not be fit (Figs. 3(b) and A1), thus supporting Faustini's old age consistent with the previous finding of Giuri et al. (2024).

Consequently, these results exclude a dataset-related issue and shift the focus of the investigation to an unknown geologic process occurring here. Thus, we examined whether basin ejecta material introduced within Faustini could account for the disturbance by providing a first-degree estimate of Imbrium, Orientale, and Schrödinger ejecta thickness using the Pike (1974) model (Table 1).

We find that the basin contributing the most material within Faustini is Imbrium, with 12^{+25}_{-8} m, while the Orientale and Schrödinger basins provided 5 m each. Taken individually, these thicknesses would reset crater populations to ~300 m and 100–200 m, respectively (Pike 1980). In Giuri et al. (2024), the disturbance occurs around craters with a 500-m diameter; thus, to fully bury or degrade all craters up to this diameter while preserving larger craters, a thickness of at least 18 m is required. Considering the limitations in the model (see Discussion section), the thickness of 12 m – from the Imbrium alone, and 18 m may be considered a good approximation within error.

4. DISCUSSION

4.1 Ejecta Thickness Uncertainties

In this work we estimate ejecta thickness primarily using the Pike (1974) model. Despite the author adjusting for the ejecta thickness at the rim of a basin or crater from McGetchin's model, leading to slightly higher estimates than both McGetchin et al. (1973) and Housen et al. (1983) – see Appendix (Tables A1 and A2), there are shortcomings with the development of the equation and consequently, with our estimates.

1. Pike (1974) assumed a vertical impact formed the basin or crater under study and that the ejecta was continuous and uniformly distributed which is not a realistic scenario for most large impacts.
2. The equation does not account for the curvature of the Moon.
3. The decay constant and transient crater diameters are estimates or models themselves (Croft 1985; Melosh 1989; Cintala & Grieve 1998; Petro & Pieters 2004; Fassett et al. 2011; Austin et al. 2024).
4. The parameters involved with basin ejecta thickness equations are poorly understood or unknown (Austin et al. 2024), thus rendering uncertainties tied to the model unquantifiable.

Table 1. Basin ejecta thickness introduced within Faustini crater using Pike (1974) equation from Imbrium, Orientale, and Schrödinger

Basin source	D (km)	Mean TC Radius (km)	α (km)	Pike constant	Pike B-value	t (km)
Imbrium	1,321	372	3,794	0.033	3	$0.012^{+0.025}_{-0.008}$
Orientale	937	198.5	2,212	0.033	3	$0.005^{+0.011}_{-0.004}$
Schrödinger	326	55.5	411	0.033	3	$0.005^{+0.007}_{-0.003}$

D refers to basin diameters after Neumann et al. (2015); Mean TC radius is the mean transient crater Radius after Wieczorek & Phillips (1999) and Petro & Pieters (2004); α is the angular distance calculated using the spherical law of cosine, and t is the ejecta thickness.

In addition, most models were developed for simple and complex craters with ejecta thickness estimates up to a distance of ~1–1.5 crater radii (McGetchin et al. 1973). For basins, complex numerical modeling is necessary to refine ejecta estimates by accounting for the extreme modification basins undergo after the impact, the degree of mixing between basin and local material, impactor and target properties, topographic shielding effects, etc. (Oberbeck et al. 1975).

Thus, questions remain about (a) whether complex crater models can reliably be applied to basin size-impacts, (b) whether distal unevenly distributed ejecta behaves similar to proximal continuous ejecta, (c) estimates of basin and transient crater diameter methods, and (d) the degree of uncertainty tied to all parameters used.

4.2 The Origin of the Disturbance

Giuri et al. (2024) found a potential disturbance or partial resurfacing in the crater statistics for Faustini and Haworth surface floor materials which was not observed in Shoemaker crater. CSFD analysis appears to record the time when this disturbance might have occurred around ~3.7 Ga ago in agreement with the Shoemaker surface material age. Consequently, an Orientale-related origin was inferred for all three crater floors given the statistically similar age with the impact event derived in a similar study (Giuri et al. 2026a). However, the ejecta thickness estimates from this work are inconsistent with the observations.

On one hand, Giuri et al. (2024) recorded a lack of 3.8 Ga Schrödinger-related deposits at the pole despite its relative geographic proximity. Instead, they were found to surround the impact, in the direction opposite to the pole, and extending to the nearside which provided support to the interpretation of Schrödinger as an oblique impact after Kring et al. (2025). Here, we find that Schrödinger introduced at least some materials within Faustini (4.5 m) potentially in agreement with an asymmetric ejecta deposition. Notably, Orientale materials are of comparable thickness to Schrödinger (~5 m). However, while the combination of Orientale's larger diameter but farther distance than Schrödinger to Faustini and its formation as an oblique impact (Guo et al. 2018; Yue et al. 2020), might reflect the modelled thickness, it does not account for the observed crater diameter at which the partial resurfacing occurs requiring a thicker deposit.

On the other hand, we find that the Imbrium contributed most of the materials within Faustini despite its distance and its established 3.92 Ga sample age (Nemchin et al. 2021). This result is in direct contradiction to the measured 3.7 Ga age in the the southern polar region in contrast to Giuri et al. (2026b) where Imbrium-aged materials (3.9–4 Ga) were found exclusively in the northern polar region.

If we consider a hypothetical cumulative ejecta thickness from all three basins within Faustini and Haworth, then a thickness of ~20 m is derived, consistent with the measured CSFD. However, an even thicker deposit would be required to account for the complete resurfacing within Shoemaker.

Thus, if we exclude a multi-basin contribution around 3.7 Ga, it is more likely that such discrepancies are (1) model-dependent, (2) reflect the complex geologic history of the southern polar region hence challenging efforts to identify the source of the disturbance, or both.

Thus, questions remain on the origin of the disturbance measured within Faustini, although alternative scenarios to be explored in future work may include topographic shielding effects, terrain elevation, mixing ratios, basin-induced seismic shaking, and potentially differential subsurface water abundance effects.

5. CONCLUSION

The lunar southern circum-polar region is the primary target for upcoming and future missions due to the presence of potential volatile species essential for exploration and human habitation. This work builds on our previous investigation into the ages and origin(s) of surface materials at the pole to better understand the geologic history of the region (Giuri et al. 2024). Here, we used (1) a ShadowCam mosaic to re-examine in greater detail the crater population within Faustini crater floor, and (2) ejecta thickness models to gain insights into the origin of the partial resurfacing recorded in our previous study. We found that despite the high-resolution of ShadowCam images, we were able to support the ancient age of the impact and that of the surface floor materials as previously derived. However, the ejecta thickness estimates produced contradicting results. We used the Pike (1974) model to estimate the amount of basin ejecta introduced into Faustini crater by the Imbrium, Orientale, and Schrödinger basins. We found that the ejecta estimates for all three basins did not convincingly support empirical evidence. Thus, it is likely that such discrepancies are a combination of model-dependent uncertainties and the complex impact history of the region.

ACKNOWLEDGMENTS

We would like to thank Mikhail Kreslavsky and an anonymous reviewer for their feedback and fruitful discussions. This work was supported by the National Aeronautics and Space Administration Lunar Reconnaissance Orbiter and ShadowCam projects.

ORCIDs

Barbara Giuri https://orcid.org/0009-0006-0187-3112
Carolyn H. van der Bogert https://orcid.org/0000-0003-2882-7037
Mark Robinson https://orcid.org/0000-0001-9964-2932

REFERENCES

Austin T, Robinson M, Mahanti P, Ejecta blankets at small craters on the Moon, Planet. Sci. J. 5, 114 (2024). https://doi.org/10.3847/PSJ/ad3827

Blewett DT, Hawke BR, Lucey PG, Taylor GJ, Jaumann R, et al., Remote sensing and geologic studies of the Schiller-Schickard region of the Moon, J. Geophys. Res. Planets. 100, 16959-16977 (1995). https://doi.org/10.1029/95JE01409

Cintala MJ, Grieve RAF, Scaling impact melting and crater dimensions: implications for the lunar cratering record, Meteorit. Planet. Sci. 33, 889-912 (1998). https://doi.org/10.1111/j.1945-5100.1998.tb01695.x

Collins WM, Grieser SA, Henriksen MR, Clark JD, Carr NF, et al., Photogrammetric processing of regional ShadowCam and LROC NAC controlled mosaics, evaluation of positional accuracies, and scientific applications, Remote Sens. 18, 525 (2026). https://doi.org/10.3390/rs18030525

Croft SK, The scaling of complex craters, J. Geophys. Res. Solid Earth. 90, C828-C842 (1985). https://doi.org/10.1029/JB090iS02p0C828

Dobrovolskis A, Ejecta patterns diagnostic of planetary rotations, Icarus. 47, 203-219 (1981). https://doi.org/10.1016/0019-1035(81)90167-6

Fassett CI, Head JW, Smith DE, Zuber MT, Neumann GA, Thickness of proximal ejecta from the Orientale Basin from Lunar Orbiter Laser Altimeter (LOLA) data: implications for multi-ring basin formation, Geophys. Res. Lett. 38, L17201 (2011). https://doi.org/10.1029/2011GL048502

Giuri B, van der Bogert CH, Hiesinger H, Ages and origins of lunar light plains, Icarus. 457, 117159 (2026a). https://doi.org/10.1016/j.icarus.2026.117159

Giuri B, van der Bogert CH, Robinson MS, Model ages of light plains and crater floors in the northern polar region, Moon, Proceedings of the 57th LPSC, The Woodlands, TX, 16-20 Mar 2026b.

Giuri B, van der Bogert CH, Robinson MS, Hiesinger H, Multiple impact sources for light plains around the lunar south pole, J. Geophys. Res. Planets. 129, e2024JE008605 (2024). https://doi.org/10.1029/2024JE008605

Gläser P, Oberst J, Neumann GA, Mazarico E, Speyerer EJ, et al., Illumination conditions at the lunar poles: implications for future exploration, Planet. Space Sci. 162, 170-178 (2018). https://doi.org/10.1016/j.pss.2017.07.006

Grieser S, Henriksen M, Wagner R, Mahanti P, Manheim M, et al., Investigation of lunar polar regions using ShadowCam mosaics, Proceedings of the 45th COSPAR Scientific Assembly, Busan, Korea,13-21 Jul 2024.

Grieser SA, Collins WM, Henriksen MR, Mahanti P, Robinson MS, ShadowCam controlled mosaics: a valuable data product for high-resolution lunar mapping, Proceedings of the 56th Lunar and Planetary Science Conference, The Woodlands, TX, 10-14 Mar 2025.

Guo D, Liu J, Head III JW, Kreslavsky MA, Lunar Orientale impact basin secondary craters: spatial distribution, size-frequency distribution, and estimation of fragment size, J. Geophys. Res. Planets. 123, 1344-1367 (2018). https://doi.org/10.1029/2017JE005446

Hartmann WK, Wood CA, Moon: origin and evolution of multi-ring basins, Moon. 3, 3-78 (1971). https://doi.org/10.1007/BF00620390

Heyer T, Iqbal W, Oetting A, Hiesinger H, van der Bogert CH, et al., A comparative analysis of global lunar crater catalogs using OpenCraterTool – an open source tool to determine and compare crater size-frequency measurements. Planet. Space Sci. 231, 105687 (2023). https://doi.org/10.1016/j.pss.2023.105687

Hiesinger H, Head III JW, Wolf U, Jaumann R, Neukum G, Ages and Stratigraphy of Lunar Mare Basalts: A Synthesis (The Geological Society of America®, Boulder, 2011).

Hiesinger H, van der Bogert CH, Michael G, Schmedemann N, Iqbal W, et al., The lunar cratering chronology, Rev. Mineral. Geochem. 89, 401-451 (2023). https://doi.org/10.2138/rmg.2023.89.10

Holsapple KA, The scaling of impact processes in planetary sciences, Annu. Rev. Earth Planet. Sci. 21, 333-373 (1993). https://doi.org/10.1146/annurev.ea.21.050193.002001

Holsapple KA, Schmidt RM, Point source solutions and coupling parameters in cratering mechanics, J. Geophys. Res. Solid Earth. 92, 6350-6376 (1987). https://doi.org/10.1029/JB092iB07p06350

Housen KR, Holsapple KA, Ejecta from impact craters, Icarus. 211, 856-875 (2011). https://doi.org/10.1016/

j.icarus.2010.09.017
Housen KR, Schmidt RM, Holsapple KA, Crater ejecta scaling laws: fundamental forms based on dimensional analysis, J. Geophys. Res. Solid Earth. 88, 2485-2499 (1983). https://doi.org/10.1029/JB088iB03p02485
Humm DC, Kinczyk MJ, Brylow SM, Wagner RV, Speyerer EJ, et al., Calibration of ShadowCam, J. Astron. Space Sci. 40, 173-197 (2023). https://doi.org/10.5140/JASS.2023.40.4.173
Humm DC, Tschimmel M, Brylow SM, Mahanti P, Tran TN, et al., Flight calibration of the LROC narrow angle camera, Space Sci. Rev. 200, 431-473 (2016). https://doi.org/10.1007/s11214-015-0201-8
Klem SM, Henriksen MR, Stopar J, Boyd A, Robinson MS, et al., Controlled LROC narrow angle camera high resolution mosaics, 45th Annual Lunar and Planetary Science Conference, The Woodlands, TX, 17-21 Mar 2014.
Kring DA, Kallenborn DP, Collins GS, Grand canyons on the Moon, Nat. Commun. 16, 1146 (2025). https://doi.org/10.1038/s41467-024-55675-z
Mahanti P, Thompson TJ, Robinson MS, Humm DC, View factor-based computation of secondary illumination within lunar permanently shadowed regions, IEEE Geosci. Remote Sens. Lett. 19, 8027004 (2022). https://doi.org/10.1109/LGRS.2022.3166809
McEwen AS, Bierhaus EB, The importance of secondary cratering to age constraints on planetary surfaces, Annu. Rev. Earth Planet. Sci. 34, 535-567 (2006). https://doi.org/10.1146/annurev.earth.34.031405.125018
McGetchin TR, Settle M, Head JW, Radial thickness variation in impact crater ejecta: implications for lunar basin deposits, Earth Planet. Sci. Lett. 20, 226-236 (1973). https://doi.org/10.1016/0012-821X(73)90162-3
Melosh HJ, Impact Cratering: A Geologic Process (Oxford University Press, New York; Clarendon Press, Oxford, 1989).
Michael GG, Kneissl T, Neesemann A, Planetary surface dating from crater size-frequency distribution measurements: poisson timing analysis, Icarus. 277, 279-285 (2016). https://doi.org/10.1016/j.icarus.2016.05.019
Michael GG, Neukum G, Planetary surface dating from crater size–frequency distribution measurements: partial resurfacing events and statistical age uncertainty, Earth Planet. Sci. Lett. 294, 223-229 (2010). https://doi.org/10.1016/j.epsl.2009.12.041
Nemchin AA, Long T, Jolliff BL, Wan Y, Snape JF, et al., Ages of lunar impact breccias: limits for timing of the Imbrium impact, Geochemistry. 81, 125683 (2021). https://doi.org/10.1016/j.chemer.2020.125683
Neukum G, Meteoritenbombardement und datierung planetarer oberflachen, Habilitation Dissertation, Ludwig-Maximilians-Universität (1983).
Neukum G, Ivanov BA, Hartmann WK, Cratering records in the inner solar system in relation to the lunar reference s ystem, Space Sci. Rev. 96, 55-86 (2001). https://doi.org/10.1023/A:1011989004263
Neumann GA, Zuber MT, Wieczorek MA, Head JW, Baker DMH, et al., Lunar impact basins revealed by Gravity Recovery and Interior Laboratory measurements. Sci. Adv. 1, e1500852 (2015). https://doi.org/10.1126/sciadv.1500852
Oberbeck VR, The role of ballistic erosion and sedimentation in lunar stratigraphy, Rev. Geophys. 13, 337-362 (1975). https://doi.org/10.1029/RG013i002p00337
Oberbeck VR, Morrison RH, Hörz F, Quaide WL, Gault DE, Smooth plains and continuous deposits of craters and basins. Proceedings of the Lunar Science Conference 5th, Houston, TX, 18-22 Mar 1974.
O'Brien P, Byrne S, Double shadows at the lunar poles, Planet. Sci. J. 3, 258 (2022). https://doi.org/10.3847/PSJ/ac9e5b
Petro NE, Pieters CM, Surviving the heavy bombardment: ancient material at the surface of South Pole-Aitken Basin, J. Geophys. Res. Planets. 109 (2004). https://doi.org/10.1029/2003JE002182
Petro NE, Pieters CM, Modeling the provenance of the Apollo 16 regolith, J. Geophys. Res. Planets. 111, E09005 (2006). https://doi.org/10.1029/2005JE002559
Petro NE, Pieters CM, The lunar-wide effects of basin ejecta distribution on the early megaregolith, Meteorit. Planet. Sci. 43, 1517-1529 (2008). https://doi.org/10.1111/j.1945-5100.2008.tb01025.x
Pieters CM, Adams JB, Mouginis-Mark PJ, Zisk SH, Smith MO, et al., The nature of crater rays: the Copernicus example, J. Geophys. Res. Solid Earth. 90, 12393-12413 (1985). https://doi.org/10.1029/JB090iB14p12393
Pike RJ, Ejecta from large craters on the Moon: comments on the geometric model of McGetchin et al., Earth Planet. Sci. Lett. 23, 265-271 (1974). https://doi.org/10.1016/0012-821X(74)90114-9
Pike RJ, Size-dependence in the shape of fresh impact craters on the Moon, in Impact and Explosion Cratering: Planetary and Terrestrial Implications, ed. Roddy DJ (Pergamon Press, New York, 1977), 489-509.
Pike RJ, Geometric Interpretation of Lunar Craters, USGS Professional Paper 1046-C (1980).
Robinson MS, Brylow SM, Caplinger MA, Carter LM, Clark MJ, et al., ShadowCam instrument and investigation overview, J. Astron. Space Sci. 40, 149-171 (2023). https://doi.org/10.5140/JASS.2023.40.4.149
Robinson MS, Brylow SM, Tschimmel M, Humm D, Lawrence SJ, et al., Lunar Reconnaissance Orbiter Camera (LROC) instrument overview, Space Sci. Rev. 150, 81-124 (2010). https://doi.org/10.1007/978-1-4419-6391-8_6

Shoemaker EM, Robinson MS, Eliason EM, The south pole region of the Moon as seen by Clementine, Science. 266, 1851-1854 (1994). https://doi.org/10.1126/science.266.5192.1851

Smith DE, Zuber MT, Neumann GA, Lemoine FG, Mazarico E, et al., Initial observations from the lunar orbiter laser altimeter (LOLA), Geophys. Res. Lett. 37, L18204 (2010). https://doi.org/10.1029/2010GL043751

Sonke A, Mahanti P, Denevi BW, Ando J, Robinson MS, et al., ShadowCam: shallower small craters in lunar permanently shadowed regions, Proceedings of the AGU Fall Meeting 2025, New Orleans, 15-19 Dec 2025.

Speyerer E, Boyd A, Wagner R, Denevi B, Robinson M, et al., Color and photometric properties of newly formed impact craters on the Moon, Planet. Sci. J. 7, 73 (2026). https://doi.org/10.3847/PSJ/ae4a06

Speyerer E, Robinson M, Carter W, Denevi B, Martin A, Interpreting the darkness: equatorial ShadowCam images shed light on permanent shadows, Proceedings of the 45th COSPAR Scientific Assembly, Busan, Korea, 13-21 Jul 2024.

Speyerer EJ, Robinson MS, Mahanti P, Denevi BW, Kinczyk MJ, et al., Interpreting the darkness: using equatorial ShadowCam observations to interpret features in permanent shadow, Proceedings of the AGU Fall Meeting Abstracts, San Francisco, CA, 11-15 Dec 2023.

Speyerer EJ, Wagner RV, Robinson MS, Licht A, Thomas PC, et al., Pre-flight and on-orbit geometric calibration of the lunar reconnaissance orbiter camera, Space Sci. Rev. 200, 357-392 (2016). https://doi.org/10.1007/s11214-014-0073-3

Trask NJ, Ranger VIII and IX, Part II. experimenters' analysis and interpretations, JPL Technical Report No. 32–800, 252–263 (1966).

Thompson TJ, Mahanti P, Robinson MS, Secondary illumination conditions at Cabeus crater, Proceedings of the 50th Annual Lunar and Planetary Science Conference No. 2132, id. 3100, The Woodlands, TX, 18-22 Mar 2019.

Watson K, Murray BC, Brown H, The behavior of volatiles on the lunar surface, J. Geophys. Res. 66, 3033-3045 (1961). https://doi.org/10.1029/JZ066i009p03033

Wieczorek MA, Phillips RJ, Lunar multiring basins and the cratering process, Icarus. 139, 246-259 (1999). https://doi.org/10.1006/icar.1999.6102

Williams JP, Mahanti P, Robinson MS, Wagner RV, Chertok M, et al., The Faustini permanently shadowed region on the Moon, Planet. Sci. J. 5, 209 (2024). https://doi.org/10.3847/PSJ/ad6f0d

Xu L, Qiao L, Xie M, Wang Y, Zhu MH, et al., Chronology, local stratigraphy, and foreign ejecta materials at the Chang'e-6 landing site: constraints on the provenance of samples returned from the Moon's farside, Geophys. Res. Lett. 51, e2024GL111311 (2024). https://doi.org/10.1029/2024GL111311

Yue Z, Yang M, Jia M, Michael G, Di K, et al., Refined model age for Orientale Basin derived from zonal crater dating of its ejecta, Icarus. 346, 113804 (2020). https://doi.org/10.1016/j.icarus.2020.113804

APPENDIX

Table A1. Ejecta thickness estimates within Haworth and Shoemaker using Pike (1974), McGetchin et al. (1973) and Housen et al. (1983) equations

Materials introduced to – from	*D* (km)	Mean TC radius (km)	*α* (km)	Pike constant	Pike *B*-value	McGetchin constant	McGetchin *B*-value	Housen constant	Housen *B*-value	Pike *t* (km)	Housen *t* (km)	McGetchin *t* (m)
To Haworth												
Imbrium	1,321	372	3,706	0.033	3	0.14	3	0.0078	2.61	$0.012^{+0.027}_{-0.008}$	0.007	$1.9^{+4}_{-1.3}$
Orientale	937	198.5	2,127	0.033	3	0.14	3	0.0078	2.61	$0.005^{+0.012}_{-0.003}$	0.003	$0.9^{+2.2}_{-0.6}$
Schrödinger	326	55.5	523	0.033	3	0.14	3	0.0078	2.61	$0.002^{+0.005}_{-0.001}$	0.001	$0.5^{+1.2}_{-0.3}$
To Shoemaker												
Imbrium	1,321	372	3,754	0.033	3	0.14	3	0.0078	2.61	$0.012^{+0.026}_{-0.008}$	0.007	$1.8^{+3.9}_{-1.2}$
Orientale	937	198.5	2,170	0.033	3	0.14	3	0.0078	2.61	$0.005^{+0.012}_{-0.003}$	0.003	$0.9^{+2}_{-0.6}$
Schrödinger	326	55.5	463	0.033	3	0.14	3	0.0078	2.61	$0.003^{+0.006}_{-0.002}$	0.002	$0.8^{+1.4}_{-0.5}$

Basin ejecta thickness introduced within Haworth and Shoemaker craters using Pike (1974), McGetchin et al. (1973) – all values in meters, and Housen et al. (1983) equations from Imbrium, Orientale, and Schrödinger. D refers to basin diameters after Neumann et al. (2015); Mean TC radius is the mean 'transient crater' radius after the diameters provided in Wieczorek & Phillips (1999) and Petro & Pieters (2004); α is the angular distance; t is the ejecta thickness in km for Pike and Housen models, and in meters for McGetchin.

$$\text{Equation used: } t = T(r/R)^{(-B)} \quad \text{(A1)}$$

Values of *T* (or 'constant' in the tables) and *B*:

Pike (1974)	$T = 0.033\ R$	$B = 3 \pm 0.5$
McGetchin et al. (1973)	$T = 0.14\ R^{0.74}$	$B = 3 \pm 0.5$
		(All values are in meters)
Housen et al. (1983)	$T = 0.0078\ R$	$B = 2.61$
		(Unreported error on *B*-value)

R is defined as the Mean TC Radius, and *r* is the distance – here defined as *α* angular distance.

To derive the thickness reported in the text and the tables here we used the following formula:

$$t = \text{X constant} \times \text{Mean TC radius} \times (\alpha / \text{Mean TC radius})^{(-\text{X n})} \quad \text{(A2)}$$

with *X* being either Pike, McGetchin (in meters), or Housen constants. All three equations rely on the correct estimation of the transient crater radius and the decay constant – which are derived differently in various other models (Fassett et al. 2011; Austin et al. 2024).

Table A2. Faustini ejecta thickness using McGetchin et al. (1973) and Housen et al. (1983) models

Materials introduced to – from	*D* (km)	Mean TC radius (km)	*α* (km)	McGetchin constant	McGetchin *B*-value	Housen constant	Housen *B*-value	McGetchin *t* (m)	Housen *t* (km)
To Faustini									
Imbrium	1,321	372	3,794	0.14	3	0.0078	2.61	$1.7^{+3.9}_{-1.2}$	0.007
Orientale	937	198.5	2,212	0.14	3	0.0078	2.61	$0.8^{+2}_{-0.5}$	0.003
Schrodinger	326	55.5	411	0.14	3	0.0078	2.61	$1^{+2}_{-0.6}$	0.002

Basin ejecta thickness introduced within Faustini crater floor from Imbrium, Orientale, and Schrödinger using McGetchin et al. (1973) – all values in meters, and Housen et al. (1983) models for comparison.

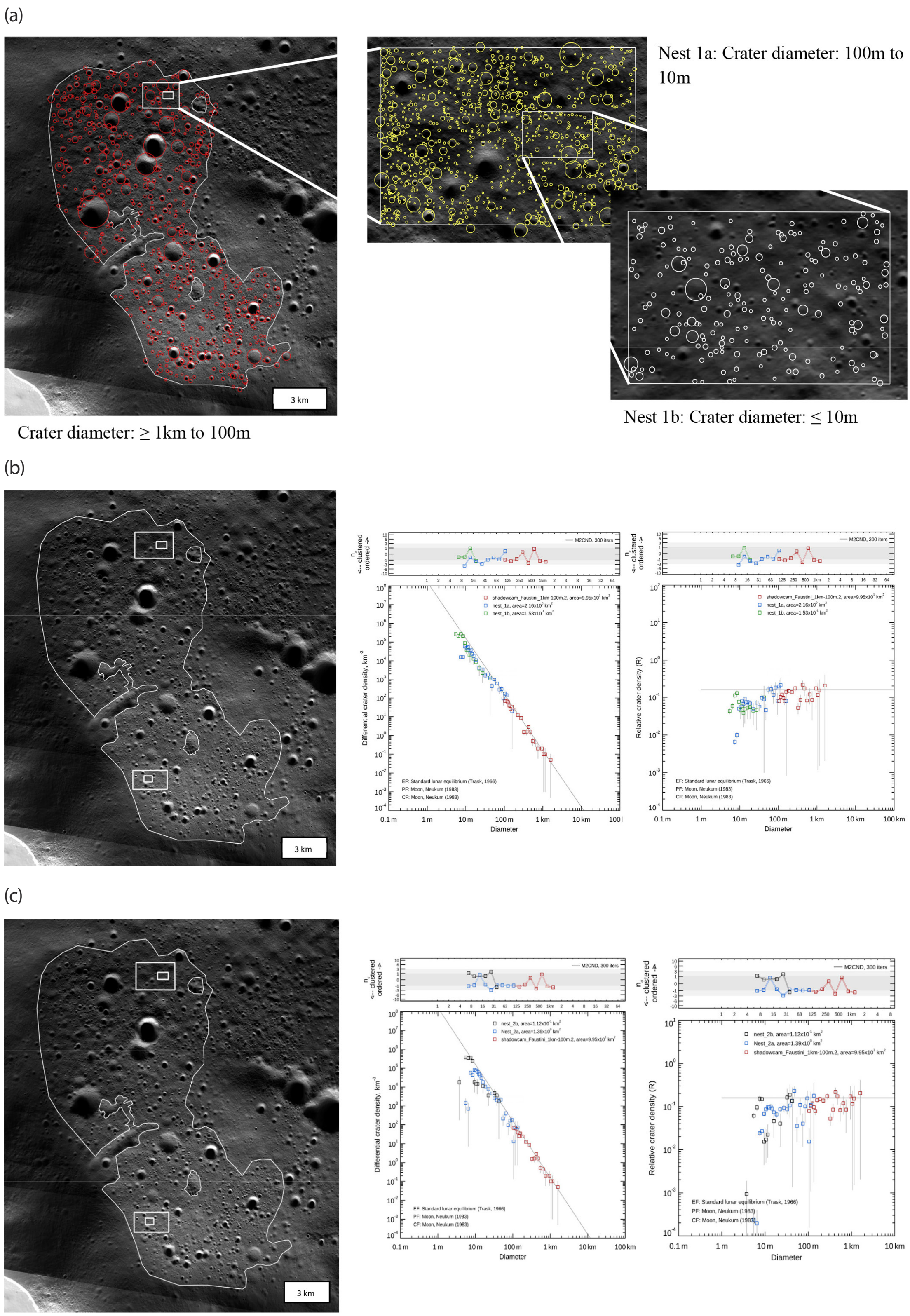

Fig. A1. Nested approach used to date Faustini crater floor and crater-size frequency distribution (CSDF) plots. (a) We adopted a nested approach with decreasing crater diameters. Our 9 main count area includes crater diameters ranging from ≥ 1 km to 100 m. Two large nests within the main count 10 areas have crater diameters of ~100 m to ≥ 10 m (Nest 1a and 2a), and within these two large nests, we selected two 11 smaller nests with remaining craters < 10 m in diameter (Nest 1b and 2b). (b) Faustini crater floor Nest 1 (top) CSFD differential and relative plots, (c) Faustini crater floor Nest 2 8 (bottom) CSFD differential and relative plots. The shapefiles from this work can be found at the following Zenodo DOI: 10.5281/zenodo.22694507.